

Radiation and Thermal Effects on Used Nuclear Fuel and Nuclear Waste Forms

Fuel Cycle Research and Development

William J. Weber

University of Tennessee, Knoxville

JC de la Garza, Federal POC
Yifeng Wang, Technical POC

Final Report

Radiation and Thermal Effects on Used Nuclear Fuel and Nuclear Waste Forms

September 20, 2016

Project No. 12-3528

Contract Number 00126749

PICS:NE Work Package NU-12_TN-UTK_-0204-02

Department of Materials Science and Engineering
University of Tennessee

This Page Intentionally Left Blank

FINAL REPORT

Project Title: Radiation and Thermal Effects on Used Nuclear Fuel and Nuclear Waste Forms

Project ID: 12-3528

Project Period: July 1, 2012 through June 30, 2016

Project Budget: \$770,000

Date of Report: September 19, 2016

Recipient: University of Tennessee, Knoxville, TN

PI: William J. Weber, 865-974-0415, wjweber@utk.edu

Co-PI: Yanwen Zhang, Yanwen@utk.edu

Contributors: Caitlin A. Taylor (PhD Student)
Joseph Graham (Postdoctoral Fellow)
Haizhou Xue (PhD Student)
Kalie Knecht (Undergraduate Student)
Maulik Patel (Research Faculty)
Miguel Crespillo Almenara (Postdoctoral Fellow)
Ke Jin (PhD Student)
Chien-Hung Chen (PhD Student)
Fenglin Yuan (Postdoctoral Fellow)

Collaborators: Yongqiang Wang, Los Alamos National Laboratory
Jeffery A. Aguiar, Idaho National Laboratory, National Renewable Energy Laboratory

This Page Intentionally Left Blank

Executive Summary

This is the final report of the NEUP project “Radiation and Thermal Effects on Used Nuclear Fuel and Nuclear Waste Forms.” This project started on July 1, 2012 and was successfully completed on June 30, 2016. This report provides an overview of the main achievements, results and findings through the duration of the project. Additional details can be found in the main body of this report and in the individual Quarterly Reports and associated Deliverables of this project, which have been uploaded in PICS-NE.

The objective of this research was to advance understanding and develop validated models on the effects of self-radiation from beta and alpha decay on the response of used nuclear fuel and nuclear waste forms during high-temperature interim storage and long-term permanent disposition. To achieve this objective, model used-fuel materials and model waste form materials were identified, fabricated, and studied.

Two model used-fuel materials, nanograined CeO_2 and ZrO_2 , were fabricated as part of this study. To complement the work on damage evolution in nanocrystalline CeO_2 and ZrO_2 during helium implantation and heavy ion irradiation, additional irradiations were performed on single crystal CeO_2 and ZrO_2 . Samples were irradiated to ion fluences corresponding to an irradiation dose ranging from 0.11 to 100 dpa (displacements per atom), which is comparable to the irradiated dose expected during interim and long-term storage. Detailed transmission electron microscopy, Rutherford backscattering and Raman spectroscopy analysis have been carried out on these irradiated materials. The critical helium concentration for formation of helium bubbles was found to be 0.15 atomic percent (at%) in these samples, which is similar to that found in ^{238}Pu -doped UO_2 . This critical helium concentration for bubble formation will be achieved in less than 100 years for MOX used fuels, in about 1000 years for high-burnup used fuels, and in 10,000 years for current commercial used nuclear fuel. In collaboration with Peking University, investigations on helium damage accumulation in yttria-stabilized zirconia (YSZ) found that the critical helium concentration to form bubbles in YSZ (3.2 at%) is much higher than in nanocrystalline ZrO_2 and CeO_2 ; the difference is speculated to be due to trapping of helium in the structural oxygen vacancy sites present in YSZ. At a peak helium concentration of 25 at%, which is not expected in any used nuclear fuel for at least 1 million years, the volumetric swelling due to bubble formation in YSZ is 27%. Comparable swelling might be expected at shorter time scales in actual spent nuclear fuel that does not have structural vacancies. While beta decay is not expected to affect the performance of used nuclear fuel, alpha decay will result in the accumulation of helium that will form helium bubbles once the helium concentration exceeds about 0.15 at% helium, which will occur within 100, 1000 or 10,000 years for MOX, high-burnup or current commercial used fuels, respectively. Due to the rim-effect in high-burnup nuclear fuels, bubble formation may be greatly accelerated and substantially higher in the rim region of nuclear fuel pellets because the local burnup is much higher (factor of two or more) than the average burnup reported for used nuclear fuel, which could lead to possible fragmentation of the outer rim on geologic time scales.

Two model waste form materials based on the pyrochlore structure, $\text{Gd}_2\text{Ti}_2\text{O}_7$ (radiation sensitive) and $\text{Gd}_2\text{Zr}_2\text{O}_7$ (radiation tolerant), have been investigated. The $\text{Gd}_2\text{Ti}_2\text{O}_7$ and $\text{Gd}_2\text{Zr}_2\text{O}_7$ samples were irradiated at room temperature to peak doses corresponding to 6 dpa in order to create a fully amorphous state in $\text{Gd}_2\text{Ti}_2\text{O}_7$ and the disordered defect-fluorite crystalline structure in $\text{Gd}_2\text{Zr}_2\text{O}_7$, which are the phase-transformed structures that will form due to self-

irradiation from alpha-decay during interim storage; consequently, it is these structures that are of interest and concern for long-term evaluation. These phase-transformed materials were implanted with helium ions to fluences equivalent to peak helium concentrations 0.1, 1.0 and 12 at% helium, which correspond to expected helium concentrations at 1000, 100,000 and over 1 million years, respectively, for a waste form containing 25 wt.% ^{239}Pu . Some of these helium implanted samples were further irradiated to simulate the response of the amorphous and disordered fluorite structures to radiation damage processes from alpha decay during long-term immobilization in a geologic repository. The combined irradiation dose (12 dpa) in these samples corresponds to 3,000 years of storage for a waste form containing 25 wt.% ^{239}Pu , 10,000 years for a waste form containing 10 wt.% ^{239}Pu , 25,000 years of storage for a waste form containing 5 wt.% minor actinides, and 1 million years of storage for a waste form containing 25 wt.% loading of commercial high-level nuclear waste. Helium bubbles did not form under any conditions for samples containing 0.1 or 1.0 at% helium, even after irradiations at 700 K. However, in the case of $\text{Gd}_2\text{Ti}_2\text{O}_7$ and $\text{Gd}_2\text{Zr}_2\text{O}_7$ samples implanted with a peak helium concentration of 12 at%, helium bubbles with diameters of 1 to 3 nm were observed in both materials. The critical helium concentration for bubble formation in amorphous $\text{Gd}_2\text{Ti}_2\text{O}_7$ was determined to be about 6 at% helium, while in the defect-fluorite $\text{Gd}_2\text{Zr}_2\text{O}_7$ the critical concentration is 4.6 at% helium. In amorphous $\text{Gd}_2\text{Ti}_2\text{O}_7$, helium bubbles were isolated and spherical. In $\text{Gd}_2\text{Zr}_2\text{O}_7$, however, helium bubbles formed chains 10-30 nm in length parallel to the surface. In summary, this work shows that $\text{Gd}_2\text{Zr}_2\text{O}_7$, often considered the most radiation resistant pyrochlore, is slightly more susceptible to formation of helium bubbles and concomitant volume swelling. Based on these results, helium bubbles are expected to form more readily in crystalline ceramic waste forms than in those that undergo radiation-induced amorphization due to alpha decay. Both of these waste forms appear to be more resistant to helium bubble formation than UO_2 , requiring nearly an order of magnitude higher helium concentration to form bubbles. This may be due to the presence of structural vacancies in $\text{Gd}_2\text{Zr}_2\text{O}_7$, similar to that observed in yttria-stabilized zirconia, and the more open structure in amorphous $\text{Gd}_2\text{Ti}_2\text{O}_7$. There may also be concerns about the ability of ion implantation to simulate helium accumulation over geologic timescales; however, reasonable agreement on the threshold helium concentration to form bubbles in helium-implanted CeO_2 and ^{238}Pu -doped UO_2 provides some validation of the approach. Unfortunately, despite many studies decades ago, no data have yet been obtained on bubble formation in ^{238}Pu -doped or ^{244}Cm -doped ceramic waste forms for comparison or benchmarking. Therefore, based on the results from this study, helium bubble formation is not expected to occur in any pyrochlore-based ceramic waste form for at least 100,000 years.

Presentations/Publications

Presentations

William J. Weber, *Simulation of Alpha-Decay Damage in Nuclear Waste Ceramics using Ion Irradiation* (Invited Paper), 2013 TMS Annual Meeting, San Antonio, TX, March 3-7, 2013.

Caitlin A. Taylor, *Alpha Decay-Induced Helium and Defect Accumulation in Ceramic Nuclear Waste Forms: Sample Synthesis and Damage Replication*, Materials Research Society Student Chapter Meeting, Clemson University, Clemson, SC, March 26, 2014.

William J. Weber, Radiation Ageing of Nuclear Waste Forms, Seminar, Sandia National Laboratories, Albuquerque, NM, May 5, 2014.

William J. Weber, *Radiation Effects in Ceramics Used for the Conditioning of Actinides*, Seminar, Jülich Research Center, Jülich, Germany, September 12, 2014.

Caitlin A. Taylor, *Experimental Determination of Helium and Defect Accumulation in Nuclear Waste Forms*, Department of Materials Science & Engineering Seminar, The University of Tennessee, Knoxville, TN, November 7, 2014.

Caitlin A. Taylor, *Experimental Determination of Helium and Defect Accumulation in Nuclear Waste Forms*, Oak Ridge Chapter of ASM Student Poster Session, Knoxville, TN, November 20, 2014.

Caitlin A. Taylor, *Experimental Determination of Helium and Defect Accumulation in Ceramic Nuclear Waste Form Materials*, Materials Research Society Fall Meeting, Boston, MA, December 2, 2014.

Caitlin A. Taylor, *Alpha Decay-Induced Helium and Defect Accumulation in Ceramic Nuclear Waste Forms*, TMS 144th Annual Meeting, Orlando, FL, March 15-19, 2015.

Joseph Graham, *Characterization of Irradiation Damage in Single Crystal Ceria by Ion Channeling and Confocal Raman Spectroscopy*, European Materials Research Society Spring 2015 Meeting, Lille, France, May 11-15, 2015.

William J. Weber, *Long-Term Effects of Helium and Damage Accumulation in Actinide Waste Forms* (Invited Paper), European Materials Research Society Spring 2015 Meeting, Lille, France, May 11-15, 2015.

Caitlin A. Taylor, *Swelling and Bubble Formation Induced by He Accumulation in Pyrochlore Nuclear Waste-Forms*, Oak Ridge Chapter of ASM Student Poster Session, Knoxville, TN, November 19th, 2015.

Caitlin A. Taylor, *Noble Gas Behavior in Nuclear Fuel and Ceramic Nuclear Waste Forms*, TMS 145th Annual Meeting, Nashville, TN, February 18th, 2016.

Caitlin A. Taylor, *Helium Behavior in Pyrochlore Type Waste-Form Materials Over Near-Term Storage and Long-Term Geological Disposal Timescales*, Materials Research Society Spring Meeting, Phoenix, Arizona, March 29th, 2016.

Publications

A. G. Perez-Bergquist, Y. Zhang, T. Varga, S. Moll, F. Namavar, and W. J. Weber, "Temperature-dependent void formation and growth at ion-irradiated nanocrystalline CeO₂-Si interfaces," *Nucl. Instrum. and Methods in Physics Research B* **325**: 66-72 (2014).

T. Wiss, J.-P. Hiernaut, D. Roudil, J.-Y. Colle, E. Maugeri, Z. Talip, A. Janssen, V. Rondinella, R. J. M. Konings, H. Matzke, and W. J. Weber, "Evolution of spent nuclear fuel in dry storage conditions for millennia and beyond," *J. Nuclear Materials* **451**: 198-206 (2014).

T. Yang, C. A. Taylor, C. Wang, Y. Zhang, W. J. Weber, J. Xiao, J. Xue, S. Yan, and Y. Wang, "Effects of He Irradiation on Yttria-Stabilized Zirconia Ceramics," *J. American Ceramic Society* **98** [4]: 1314-1322 (2015).

C.A. Taylor, M.K. Patel, J.A. Aguiar, Y. Zhang, M.L. Crespillo, J. Wen, H. Xue, Y.Q. Wang, and W.J. Weber, "Bubble formation and lattice parameter changes resulting from He irradiation of defect-fluorite Gd₂Zr₂O₇," *Acta Materialia* **115**: 115-122 (2016).

C. A. Taylor, M. K. Patel, J. A. Aguiar, Y. Zhang, M. L. Crespillo, J. Wen, H. Xue, Y. Q. Wang, and W. J. Weber, “Combined Effects of Radiation Damage and He Accumulation on Bubble Nucleation in $\text{Gd}_2\text{Ti}_2\text{O}_7$,” *Journal of Nuclear Materials* **479**: 542-547 (2016).

Final Technical Report

1. Overview and Background:

Used nuclear fuel and nuclear waste forms will be exposed to radiation and thermal effects during interim storage and permanent disposal. While nuclear fuel undergoes significant restructuring during high temperature irradiation in the reactor core, the radiation and thermal environment for out-of-reactor used nuclear fuel, as well as for nuclear waste forms, is substantially different. During near-term interim storage (up to several hundred years), both used nuclear fuel and waste forms will be subjected to a high-temperature thermal environment produced primarily from beta-decay of short-lived fission products. After this, radiation damage and helium accumulation from alpha decay of actinides at near ambient conditions will be dominant for millions of years, with limited damage recovery or helium release. While there has been decades of studies on the restructuring of nuclear fuel during in-reactor irradiation to various levels of burnup, there have been few studies on the long-term restructuring of used fuel. In used nuclear fuels, completely different radiation damage processes will dominate for near-term storage and long-term geologic disposal, and the structure and properties of aged nuclear fuel in a thousand or several hundred thousand years may not be well represented by today's characterization of used fuel [1,2], and assessment of long-term behavior requires a rigorous scientific approach [3]. Self-radiation damage from alpha decay in UO_2 , as shown in Fig. 1, and many crystalline ceramic waste forms leads to the evolution of microstructure, such as dislocation loops and helium bubbles, at ambient temperature. While the accumulation of helium from alpha decay will lead to helium bubble formation in nuclear waste forms, it may lead to both helium bubble formation and growth of existing fission gas bubbles in used nuclear fuel. Several representative doses for used nuclear fuel [4] are shown in Fig. 2 as a function of time out-of-reactor, along with the corresponding accumulated helium content. Included in Fig. 2 is the helium content (2500 appm helium) where the formation of helium bubbles has been observed due to alpha decay in ^{238}Pu -doped UO_2 [4]. The conditions for helium bubble formation are not well known, but based on the data in Fig. 2, the onset of helium bubble formation could

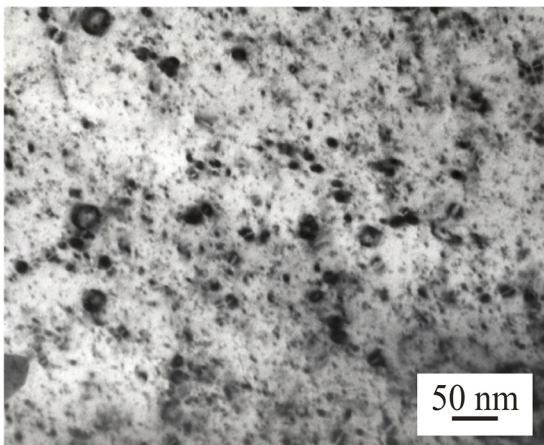


Fig. 1. Microstructure in ^{238}Pu -doped UO_2 after 6×10^{18} α -decays/g [4].

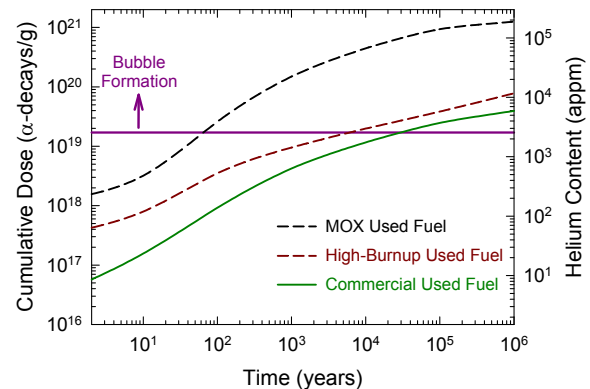


Fig. 2. Cumulative dose in high burnup (100 GWd/tM), MOX (60 GWd/tM) and typical commercial (40 GWd/tM) used fuels, along with the dose for observable helium bubble formation in UO_2 [4].

occur in less than 100 years (i.e., during interim storage) in MOX nuclear fuels, after about a 6,000 thousand years in high-burnup nuclear fuels or after 25,000 years in current commercial used nuclear fuel. Whether existing microstructures in current-generation used nuclear fuel (e.g., precipitates or sub-grain structures) or engineered microstructures in future fuels (e.g., nano-grain sizes [5]) and waste forms inhibit damage accumulation and helium bubble formation requires investigation. In addition to helium bubble formation, radiation-induced amorphization is observed at lower doses ($\sim 5 \times 10^{18}$ α -decays/g) in many ceramics proposed for immobilizing actinides [6,7]. Since helium release and phase separation are more likely in amorphous structures, the long-term effects of the radiation-induced amorphous structure on helium retention, bubble formation, and phase separation should be investigated.

During the interim storage thermal period, the combined effects of radiation and high temperatures from beta and alpha decay can lead to phase instabilities, charge imbalance, and redistribution of fission products and actinides. Predicting the structural and chemical response of used nuclear fuel and waste forms during this high thermal and radiation stage are critical to establishing the benchmark structures on which to model their long-term structural and chemical evolution due to continued self-radiation damage and helium accumulation from alpha decay of actinide elements. In order to develop the necessary understanding and predictive models, improved experimental approaches and modeling methods need to be developed, and well-designed separate effect experiments are essential for model validation. Since timescales range from hundreds to millions of years, all performance models must be validated using laboratory-scale experiments that are highly accelerated in time [1-3]. While using short-lived actinides, such as ^{238}Pu and ^{244}Cm , to simulate alpha-decay damage processes on accelerated time scales is attractive, the high costs, high radioactivity and long timeframe for such studies (tens of years) have limited the use of this approach in recent decades. Instead, under this project, the experimental approach has been based on irradiations with energetic helium and heavy ions to provide a cost-effective approach for investigating the effects of irradiation on model used fuel and waste form materials over a wide range of temperatures under controlled and separable irradiation conditions, without producing radioactive samples.

Under this project, systematic investigations have been conducted on the irradiation response of model used fuel and waste form materials over a range of relevant temperatures. Alpha-decay damage will largely self-heal in used fuel at the highest temperatures expected during interim storage ($<600^\circ\text{C}$), as indicated in Fig. 3 for thermal recovery of alpha-decay damage in mixed $\text{PuO}_2\text{-UO}_2$ [8]; however, alpha-decay damage will increasingly accumulate as the storage temperature decreases over the first few hundred years. During interim storage (several hundred to 1,000 years), used fuel and waste forms will experience alpha-decay doses that could range from 10^{18} to 10^{20} α -decays/g, depending on fuel type or actinide content (Fig. 2). These doses are equivalent to doses of 0.1 to 10 displacements per atom (dpa) [6] and accumulated helium concentrations of 100 to 20,000 appm (Fig. 2). Once in geologic isolation, the behavior of used nuclear fuel and nuclear waste forms will need

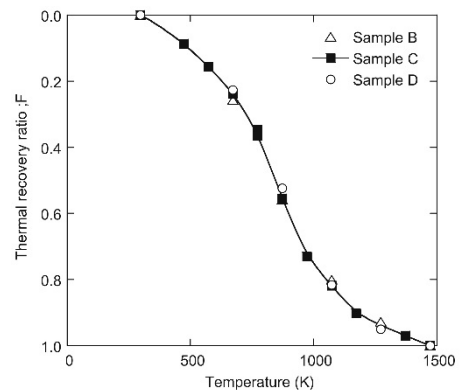


Fig. 3. Thermal recovery of α -decay damage in a simulated MOX used fuel [8].

to be predictively modeled over long time periods, extending out to 100,000 years or more. During this extended period, used fuel and waste forms will be at ambient temperatures and will experience alpha-decay doses that range from 10^{19} to 10^{21} α -decays/g, depending on fuel type (Fig. 2), which are equivalent to doses from 1 to 100 dpa, respectively, and helium concentrations up to 200,000 appm (20 at%). Under such conditions, helium bubbles are well known to form in natural minerals, as illustrated in Fig. 4.

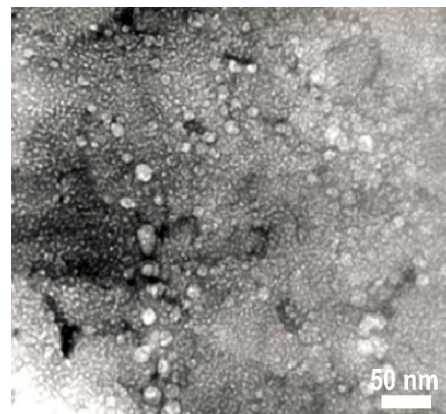


Fig. 4. Helium bubbles from alpha decay in natural thorianite (ThO_2) after 550 million years [4].

Under this project, studies of such long-term effects have been conducted primarily under ambient repository temperatures using heavy-ion irradiation and helium implantation to investigate alpha-decay doses equivalent to several hundred thousand years. To minimize handling of radioactive materials, model used-fuel materials have been used, such as CeO_2 , which has been widely and successfully used as a non-radioactive surrogate in the study of in-reactor radiation damage, restructuring and fission gas diffusion in UO_2 -based nuclear fuels [9,10,11]. Pyrochlore structures, with the formula $\text{A}_2\text{B}_2\text{O}_7$, can readily accommodate various actinides at the A and B sites [7], and two model waste form materials based on the pyrochlore structure, $\text{Gd}_2\text{Ti}_2\text{O}_7$ (radiation sensitive) and $\text{Gd}_2\text{Zr}_2\text{O}_7$ (radiation tolerant), have been studied under this project. While radiation resistance of these pyrochlores has been studied at relatively low doses [7], their response to helium accumulation and continued irradiation is unknown. The susceptibility of these materials to helium bubble formation has not been studied. Even in the case of the zirconate pyrochlores, which are highly resistant to radiation-induced amorphization, dislocation loop formation, radiation-induced segregation and cavity formation are expected at much higher doses, similar to the behavior in UO_2 .

The heavy irradiations have been performed at the University of Tennessee's Ion Beam Materials Laboratory (UTK-IBML) [12], which has provided students and post docs with hands-on training related to radiation damage processes and experimental design. This facility has the capability of irradiating samples separately or sequentially with heavy ions and helium ions. Helium ion implantations were performed at Los Alamos National Laboratory Ion Beam Materials Laboratory (LANL-IBML). This research has also closely collaborated with ongoing international studies on self-radiation damage in ^{238}Pu -doped UO_2 and $\text{UO}_2\text{-PuO}_2$ [4]. Data from such studies have provided benchmarks for experimental and modeling efforts.

2. Experimental Accomplishments

2.1. Used Nuclear Fuel

2.1.1. Helium Bubble Formation

Two model used-fuel materials, nano-grained CeO_2 and ZrO_2 , were fabricated for study [13,14], and the typical nano-grained structure is illustrated in Fig. 5. Samples of nano-grained CeO_2 and

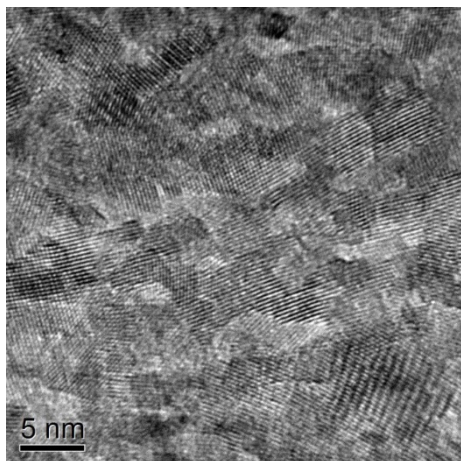


Fig. 5. Nanocrystalline grain structure in CeO₂ film prepared by ion-beam assisted deposition.

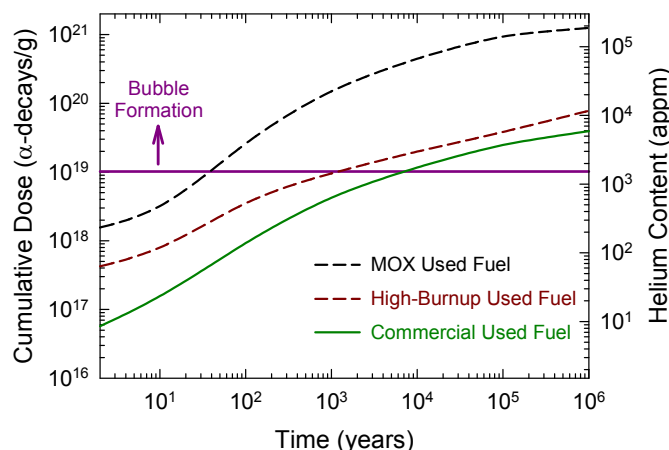


Fig. 6. Cumulative dose and helium content in used nuclear fuels (from Fig. 2) and predicted condition from this work for formation of helium bubbles.

ZrO₂ samples were implanted with 65 keV He⁺ ions at the LANL-IBML. The CeO₂ samples were implanted to ion fluences of 1×10^{15} ions/cm² and 3×10^{15} ions/cm², while ZrO₂ samples were implanted to ion fluences of 1×10^{15} ions/cm², 3×10^{15} ions/cm², and 1×10^{16} ions/cm². All helium-implanted CeO₂ and ZrO₂ samples were investigated via transmission electron microscopy (TEM) using a Phillips CM 200 TEM/STEM operating at 200 kV. Rare helium bubbles of 2 to 3 nm in diameter were observed in the CeO₂ sample at 1×10^{15} ions/cm² (500 appm helium). Some bubbles of up to 7 nm in diameter were observed in the CeO₂ sample at 3×10^{15} ions/cm² (1500 appm helium). No bubbles were observed in the ZrO₂ sample at 1×10^{15} ions/cm²; whereas the samples irradiated at 3×10^{15} ions/cm² (1500 appm helium) and 1×10^{16} ions/cm² (5,000 appm helium) showed bubble-like defects of 2 to 4 nm in diameter. The threshold helium concentration of 1500 appm helium for observable bubbles in nano-grained CeO₂ and ZrO₂ is similar to that found for ²³⁸Pu-doped UO₂ (i.e., about 2500 appm) [4]. The helium concentration of 1500 appm (0.15 at%) is what would be expected in about 100 years for MOX used nuclear fuel, 1000 years for high-burnup UO₂ used nuclear fuel and 10,000 years for current commercial used nuclear fuel, as shown in Fig. 6. Due to the rim-effect in high-burnup nuclear fuels, bubble formation may be greatly accelerated and substantially higher in the rim region of nuclear fuel pellets because the local burnup is much higher (factor of two or more) than the average burnup reported for used nuclear fuel [15]. This could lead to the opening of grain boundaries, as observed in aged ²³⁸Pu [16], and possible fragmentation of the rim region in high-burnup used nuclear fuel on geologic time scales.

In collaboration with Peking University, the effects of helium implantation at room temperature on yttria-stabilized zirconia (YSZ) have been studied. The results demonstrate that the damage accumulation behavior is similar for polycrystalline and single crystal YSZ, and the damage accumulation occurs as a multistep process, similar to that observed in single crystal CeO₂ under this project (discussed below). The first stage of this process is associated with the accumulation of point defects. After a dose of about 0.45 dpa, the clustering of defects is dominant in the second stage. In the third stage, dislocation loops grow and become a network of tangled dislocations. Helium bubbles were observed to begin forming at a helium implantation fluence of

5×10^{16} helium ions/cm², which corresponds to a peak helium concentration of 3.2 at%. Swelling was determined from the step height difference between the implanted and masked (unirradiated) regions. The swelling due to bubble formation was about 27% at a helium ion fluence of 4×10^{17} helium ions/cm², as shown in Fig. 7. The bubbles were observed to preferentially form along grain boundaries, as illustrated in Fig. 8 (a). Above a fluence of 2×10^{17} surface blistering is apparent, as illustrated in Fig. 8 (b). The results of this collaboration have been published [17].

The critical helium concentration (3.2 at%) to form bubbles in YSZ is much higher than the concentration (0.15 at%) observed under this project to form helium bubbles in nanocrystalline CeO₂ and ZrO₂ or that (0.25 at%) in ²³⁸Pu-doped UO₂ [4]; the difference is attributed to trapping of helium in the structural oxygen vacancy sites present in YSZ.

2.1.2. Defect Accumulation

To complement the work on damage evolution in nanocrystalline CeO₂ and ZrO₂ during helium implantation and heavy ion irradiation, additional irradiations were performed to identify the irradiation induced defect species in single crystal CeO₂ films. Samples were irradiated at the UTK-IBML with 2 MeV Au²⁺ ions at fluences ranging from 8.5×10^{13} to 8.2×10^{16} ions/cm². These fluences cover a dose range of 0.11 to 100 dpa, which corresponds to the irradiated dose in expected during interim and long-term storage. Subsequent ion channeling and Rutherford Backscattering Spectrometry (RBS) measurements were conducted with 3.5 MeV He normal to

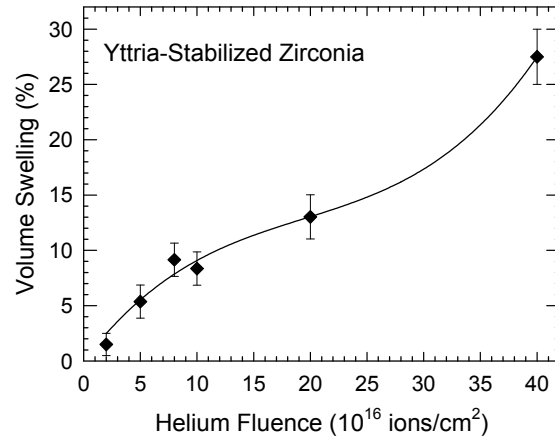


Fig. 7. Volume swelling as a function of implanted helium fluence in yttria-stabilized zirconia (adapted from Reference 17).

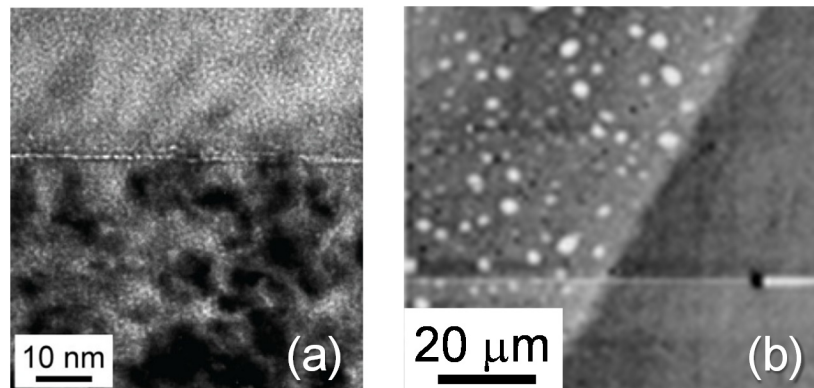


Fig. 8. Helium implanted yttria-stabilized zirconia: (a) helium bubbles along grain boundary (5×10^{16} helium ions/cm²); (b) surface blistering (2×10^{17} helium ions/cm²) near boundary between implanted (left) and unimplanted (right) region (adapted from Reference 17).

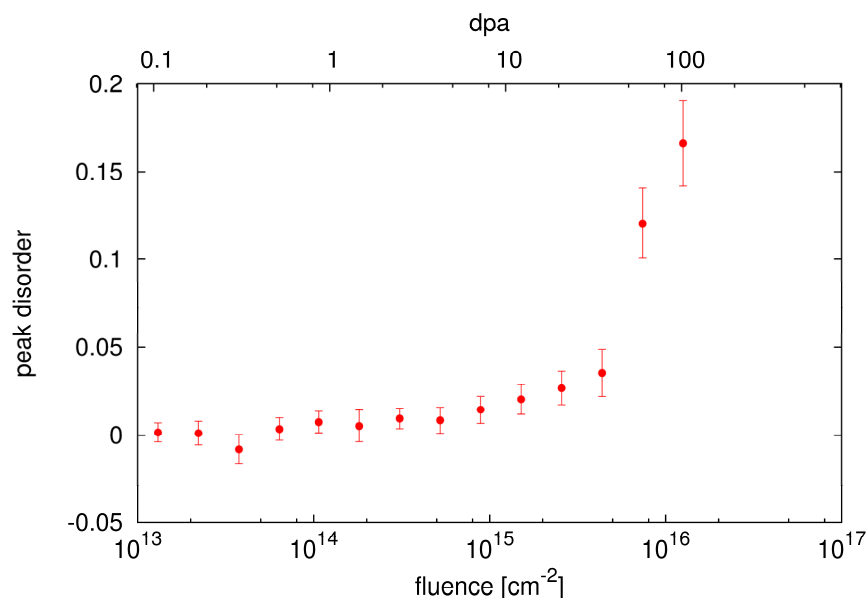


Fig. 9 Peak disorder vs. dose as calculated from Rutherford backscattering spectra along the $\langle 100 \rangle$ direction in single crystal CeO_2 irradiated with 2 MeV Au^+ . The onset of disordering is only measurable above 10 dpa.

the film surface to determine the peak disorder on the Ce sub-lattice at each ion fluence. Subsequent ion channeling and Rutherford Backscattering Spectrometry (RBS) measurements were conducted with 3.5 MeV He normal to the film surface to determine the peak disorder on the Ce sub-lattice at each ion fluence. The measured disorder accumulation as a function of irradiation dose is shown in Fig. 9. The behavior over the dose range from 0.1 to 2 dpa is similar to that expected during interim storage conditions.

Following the RBS channeling measurement, confocal Raman spectroscopy was also used to characterize the defect accumulation behavior. In evaluating the experimental results from the Raman measurements, the line-shape corresponding to the Raman active F_{2g} vibrational mode was found to show a sensitive dependence to irradiation; even at modest doses (0.1 dpa and below). This is in contrast to Rutherford backscattering spectrometry (RBS) measurements, which were only able to detect statistically significant accumulations of disorder at doses in excess of 5 dpa. These Raman results are shown in Figs. 10 and 11.

To provide physical interpretations of these results, molecular dynamics (MD) calculations were performed in order to simulate perturbations to the phonon density of states

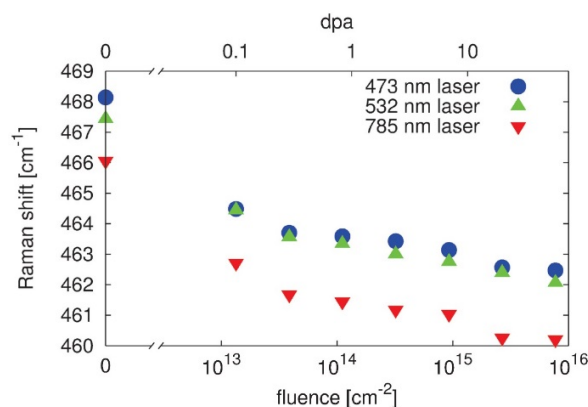


Fig 10. The Raman line shift of the F_{2g} mode as a function of ion fluence and dpa.

(DOS) due to various defect clusters (e.g. vacancies, interstitials, binary clusters). However, in partially disordered crystals, Raman scattering only excites near-zone-center phonons. This makes the calculation of the Raman signal difficult from thermodynamic ensemble-averaged quantities obtained using MD. An alternative approach based on calculation of the phonon dispersion curves was found to be successful in reproducing the changes in line shape. The computational demands of this approach are comparatively small, and the approach is outlined below.

Phonon dispersion curves were calculated from a rigid ion model consisting of nearest neighbor interactions between Ce atoms on the Ce sub-lattice, O atoms on the O sub-lattice and between Ce and O atoms. The model is described in detail elsewhere [18,19]. The short-range force-constant matrix Φ for each set of nearest neighbor interactions is based on the following sets of 3x3 matrices:

$$\Phi(Ce - Ce) = \begin{bmatrix} \alpha_1 & \beta_1 & \beta_1 \\ \beta_1 & \alpha_1 & \beta_1 \\ \beta_1 & \beta_1 & \alpha_1 \end{bmatrix}$$

$$\Phi(Ce - O) = \begin{bmatrix} \alpha_2 & 0 & 0 \\ 0 & \beta_2 & \gamma_2 \\ 0 & \gamma_2 & \beta_2 \end{bmatrix} \quad (1)$$

$$\Phi(O - O) = \begin{bmatrix} \alpha_3 & 0 & 0 \\ 0 & \beta_3 & 0 \\ 0 & 0 & \beta_3 \end{bmatrix}$$

All other matrices are given by rotations of these into symmetrically equivalent directions. A dipole term is added to the force constant matrix to account for long-range Coulombic forces

$$\Phi(i, j) = -\frac{q_i q_j}{R_{ij}^3} \left\{ 3 \frac{R_{ij} R_{ij}}{R_{ij}^2} - 1 \right\} \quad (2)$$

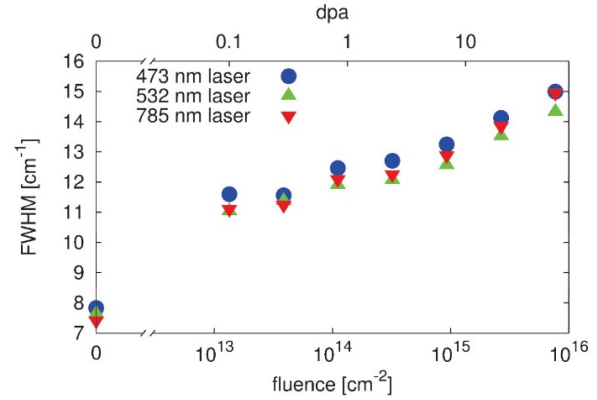


Fig. 11. The Raman line width as a function of ion fluence and dpa.

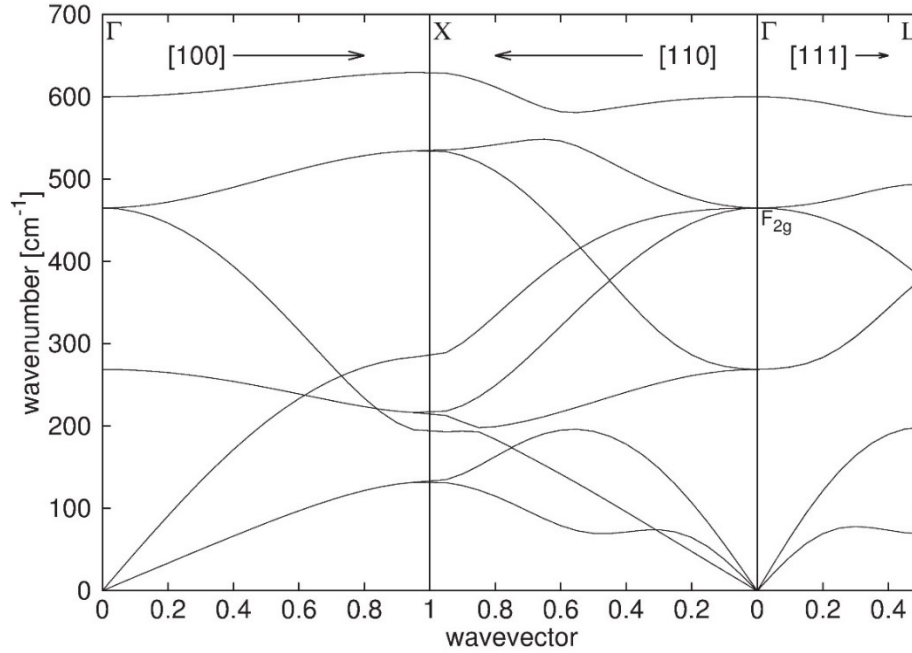


Fig. 12. Phonon dispersion curves for CeO₂ along high symmetry directions.

where q_i is the charge of ion i and \mathbf{R}_{ij} is the vector between the equilibrium positions of ion i and j . The values used for $\alpha_1, \beta_1, \alpha_2, \beta_2, \gamma_2, \alpha_3, \beta_3$ and q_i are taken from Nakajima et al. [19] and were fit to infrared reflectivity, Raman and elastic constant data. The calculated dispersion curves along high symmetry directions are shown in Fig. 12.

In a perfect crystal, the atomic vibrations corresponding to a single vibrational mode are correlated over an infinite range (neglecting electron-phonon and phonon-phonon coupling). Furthermore, a visible or IR laser has a wavelength large compared to the lattice parameter. This leads to the phonon wavevector selection rule $\mathbf{q}=0$. In other words, the Raman spectrum should have peaks at wavenumbers corresponding to the points where the Raman active optical phonon branches intersect the Brillouin zone-center. In CeO₂ this corresponds to a triply degenerate F_{2g} peak occurring at $\omega = 465 \text{ cm}^{-1}$.

For a material with defects, atomic vibrations are only correlated over a certain length. Due to repeated scattering at defects, a phonon only propagates a certain distance before being damped in the scattering medium. Richter et al. [20] assumed that the displacement-displacement correlation function is Gaussian in shape:

$$\exp\left(-\frac{2r^2}{L^2}\right) \quad (3)$$

where r is the distance between the two points where the correlation function evaluated. L is the

correlation length. The Raman intensity, $I(\omega)$, at each wavenumber, ω , in a disordered material, characterized by a given correlation length, can be expressed as:

$$I(\omega) \propto \int \exp\left(-\frac{q^2 L^2}{4}\right) \frac{d^3 q}{[\omega - \omega(q)]^2 + [\Gamma_0/2]^2} \quad (4)$$

Γ_0 is the intrinsic line width of the initially defect free crystal. This model has been used to predict changes in line shape in Raman spectra in microcrystalline Si [20], fused silica [21], irradiated GaAs [22], and graphene [23]. Equation (4) was evaluated using different values of L and a table of $\omega(q)$ values for the F_{2g} branch was generated from the dispersion curve calculations. As with the experimental data, Lorentzian curves were fitted to the peaks resulting in values of the Raman peak shift $\Delta\omega$ and line width Γ parameterized by L , as shown in Fig. 13. The model (dotted curve) was found to be in reasonable agreement with the experimental data when the crystal is assumed to be initially disorder free (infinite L). Some improvement in the agreement can be made if the initial correlation length is chosen to be large but finite (50 lattice parameters - see Fig. 13 dashed line). This is reasonable considering there is always a certain level of disorder in the material, and phonon-phonon scattering might not be completely negligible at room temperature. It should be mentioned, however, that there are also uncertainties in the phonon dispersion curves that could lead to discrepancies between the model and experimental data.

With the model verified, it is useful to consider the dependence of correlation length with dose. In fact, $1/L^3$ is a more interesting quantity because, in principle, it is closely related to the density of phonon scattering centers (such as defects) and the scattering cross sections of said centers. This quantity is shown as a function of ion fluence and dpa in Fig. 14. Clearly it increases monotonically in a manner consistent with expectation. Indeed, there appears to be a change in the rate of increase around 10 dpa. This might be related to the transition between stage 1 and stage 2 damage evolution evident from the previous RBS measurements that are shown in Fig. 8. An important point to mention is that the Raman measurement appear to be sensitive to disorder at doses <10 dpa but less sensitive above 10 dpa (compared to RBS). One potential explanation of this is that while the RBS data only indicate disorder on the Ce sub-lattice, the F_{2g} mode consists of vibrations on the O sub-lattice only. Therefore, the data may indicate a difference in the accumulation

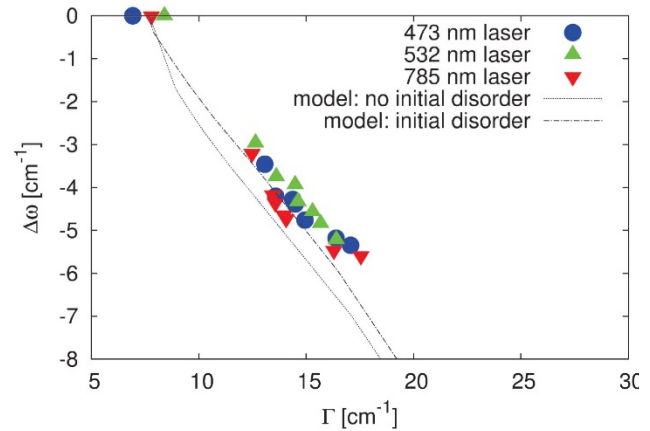


Fig. 12. Raman line shift (measured relative to virgin sample) vs. line width experimental data and modeling prediction. The dotted line corresponds to an assumption that the virgin sample has no initial disorder while the dashed line corresponds to a model where the virgin sample has a small amount of disorder present ($L = 270\text{\AA}$).

rates of stage 2 disorder between each sub-lattice. Alternatively, while the defect density may increase rapidly in stage 2, the phonon-defect scattering cross sections for defects present in stage 2 are substantially smaller than those in stage 1.

One outcome of these results is that the Raman measurements are found to be complimentary to RBS measurements, both in that they are sensitive in different dose regimes (RBS: >10 dpa, Raman: <10 dpa) and that, in theory, they are sensitive to different sub-lattices.

2.2. Nuclear Waste Forms

Pyrochlore structured ceramics ($A_2B_2O_7$) represent a class of potential waste form structures for the immobilization of actinides. Both titanate pyrochlores ($A_2Ti_2O_7$), which readily undergo radiation-induced amorphization (radiation sensitive), and zirconate pyrochlores ($A_2Zr_2O_7$), which readily undergo an order-disorder transformation, but remain crystalline (radiation tolerant), are of interest [7]. The model waste form materials for long-term performance evaluation are the irradiation-induced amorphous structure of $Gd_2Ti_2O_7$ and the defect-fluorite structure of $Gd_2Zr_2O_7$ that will form during interim storage, unaffected by any existing thermal environment, after several hundred to a thousand years storage, as shown in Figs. 15 and 16.

2.2.1. Sample Preparation

Under this project, $Gd_2Ti_2O_7$ and $Gd_2Zr_2O_7$ samples were prepared either by Hot Iso-static Pressing (HIP) to near theoretical density or by cold-pressing and sintering. The samples were

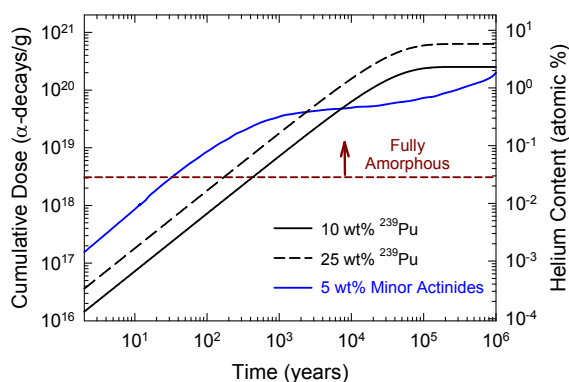


Fig. 15. Cumulative dose and helium content in $Gd_2Ti_2O_7$ as a function of time for various waste loadings.

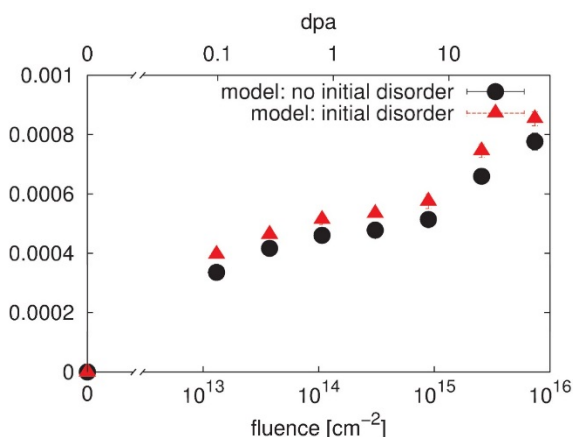


Fig. 14. Phonon correlation length L dependence on ion fluence and dpa. $1/L^3$ is plotted here because it has an obvious connection to the density of scattering sites in the material and therefore correlated with the defect density.

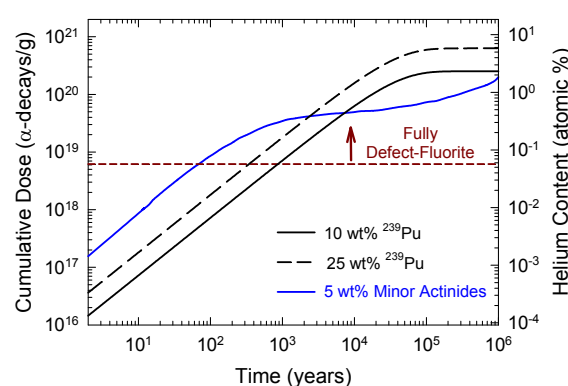


Fig. 16. Cumulative dose and helium content in $Gd_2Zr_2O_7$ as a function of time for various waste loadings.

cut using a diamond saw to thicknesses of about 1.5 mm and polished using diamond lapping sheets down to 1 μm . The polishing damage was removed using a colloidal silica solution. The objective of the experiments is to simulate helium accumulation and radiation damage in model nuclear waste ceramics ($\text{Gd}_2\text{Zr}_2\text{O}_7$ and $\text{Gd}_2\text{Ti}_2\text{O}_7$) over interim and long-term storage periods.

2.2.2. Irradiation and Implantation Conditions

Prior to helium implantation, polished $\text{Gd}_2\text{Ti}_2\text{O}_7$ and $\text{Gd}_2\text{Zr}_2\text{O}_7$ samples were irradiated at the UTK-IBML with 7 MeV Au ions to a fluence of 2.2×10^{15} ions/ cm^2 at room temperature, corresponding to a peak damage of 6 dpa, to create a fully amorphous state in $\text{Gd}_2\text{Ti}_2\text{O}_7$ and the disordered defect-fluorite structure in $\text{Gd}_2\text{Zr}_2\text{O}_7$, which are the structures of interest and concern for long-term evaluation. In the case of $\text{Gd}_2\text{Ti}_2\text{O}_7$, irradiating with 7 MeV Au created a thick amorphous layer ($\sim 2 \mu\text{m}$ thick), as shown in Fig. 17, representative of the damage state present inside a waste form prior to the formation of helium bubbles. Similarly, irradiating $\text{Gd}_2\text{Zr}_2\text{O}_7$ with 7 MeV Au ions to a fluence of 2.2×10^{15} ions/ cm^2 produced a thick disordered defect-fluorite layer representative of the damage state present after interim storage. These samples were subsequently implanted at the LANL-IBML with 200 keV helium ions to fluences of 2×10^{15} (0.1 at% He) and 2×10^{16} (1 at% He) ions/ cm^2 , corresponding to the expected helium concentrations at 1000 and 10,000 years, respectively, in a waste form containing 25 wt% ^{239}Pu , as illustrated in Figs. 15 and 16. Some of these helium implanted samples were further irradiated with 7 MeV Au^{3+} within the UTK-IBML to an additional ion fluence of 2.2×10^{15} ions/ cm^2 at room temperature in order to simulate the response of the amorphous and disordered fluorite structures to the accumulation of additional alpha-recoil damage from alpha decay during long-term immobilization in a geologic repository. The combined irradiation dose (12 dpa) in these samples corresponds to 3,000 years of storage for a waste form containing 25 wt% ^{239}Pu , 10,000 years of storage for a waste form containing 10 wt% ^{239}Pu , 50,000 years of storage for a waste form containing 5 wt% minor actinides, and 1 million years of storage for a waste form containing 25 wt% loading of commercial high-level nuclear waste. Additional $\text{Gd}_2\text{Ti}_2\text{O}_7$ and $\text{Gd}_2\text{Zr}_2\text{O}_7$ samples were irradiated with 7 MeV Au, as detailed above, and implanted with 65 keV helium ions at the LANL-IBML to a fluence of 2×10^{17} ions/ cm^2 . This He ion fluence corresponds to a peak helium content of ~ 12 at%. Implanting helium at an energy of 200 keV or 65 keV produces a helium concentration peak shallower than the Au concentration peak, and well within the Au damaged layer. Thus, in both cases, the helium is entirely contained in the damaged, amorphous layer for $\text{Gd}_2\text{Ti}_2\text{O}_7$ and the damaged, defect-fluorite regions for $\text{Gd}_2\text{Zr}_2\text{O}_7$, as well as within the region where the chemical compositions of $\text{Gd}_2\text{Ti}_2\text{O}_7$ and $\text{Gd}_2\text{Zr}_2\text{O}_7$ remain mostly unaffected by the implanted Au.

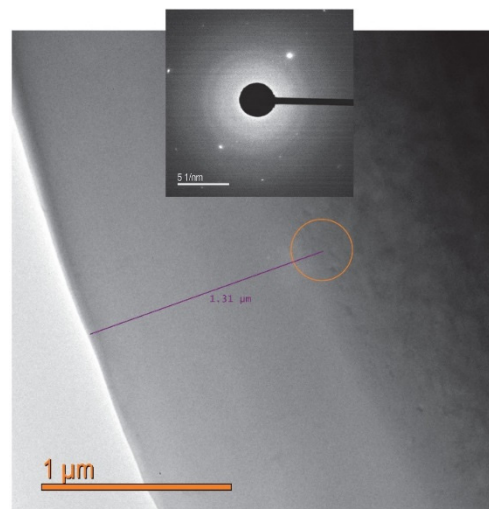


Fig. 17. TEM images and electron diffraction pattern of $\text{Gd}_2\text{Ti}_2\text{O}_7$ irradiated with Au ions. Orange circle indicates region where SAED pattern was taken at the amorphous-crystalline interface.

2.2.3. Characterization

The Au-irradiated (defect-fluorite) $\text{Gd}_2\text{Zr}_2\text{O}_7$ samples were characterized using GXRD to establish a baseline lattice parameter for the defect-fluorite structure. Measurements were performed using a PANalytical Empyrean X-ray diffractometer equipped with a focusing beam mirror, Ni filter, $1/8^{\text{th}}$ divergence slit, 4 mm mask and 0.04 rad Soller slits on the incident beam side and 0.04 rad Soller slits, a 0.09 parallel plate collimator and a Xe gas proportional detector on the diffracted beam side. Data were compared to the parallel beam configuration, and it was determined that no 2θ shift needed to be applied to account for sample displacement. After the helium implantations, GXR scans were collected for all samples using a PANalytical X'Pert³ X-ray diffractometer equipped with a $1/16^{\text{th}}$ divergence slit, a parallel beam mirror, 0.02 rad Soller slits and a 4 mm mask on the incident beam side, and a 0.09 parallel plate collimator, 0.02 rad Soller slits and a Xe gas proportional detector on the diffracted side. Various grazing angles for the helium implanted samples were chosen to probe different regions of the helium profile. X-ray penetration depths corresponding to each grazing angle for each set of samples were visually compared to the SRIM predicted He and Au profiles. X-ray penetration depths were calculated based on total external reflection theory using bulk density values. Lattice parameters were calculated by fitting the (220) and (311) peaks because these had the highest 2θ positions with resolvable peaks. Percent strain was calculated using the formula, $(a - a_0) / a_0 \times 100$. All XRD measurements were performed at the UTK-JIAM (Joint Institute for Advanced Materials) X-ray Diffraction Facility, and all GXR peak were fit using a pseudo-Voigt function in the software CMPR and errors were propagated from the standard deviation provided by the fit [24].

Transmission electron microscopy (TEM) was utilized to characterize the damage structure of each irradiated sample, as well as quantify any helium bubble formation. Due to difficulties preparing cross-sections that were uniformly thin over a $\sim 3 \mu\text{m}$ depth from the surface by hand polishing, cross-sectional lamellae of approximately 90-115 nm thickness were lifted out using the focused ion beam (FIB) sample preparation technique. The sample was intentionally left thick in order to preserve the critical thickness needed to resolve dislocations and to maximize the number of helium bubbles preserved within the sample thickness. An FEI Nova 200 Nanolab Dual Beam focused ion beam was used in preparing samples. The sample surface was protected from ion beam damage by using a 5 keV electron beam and a gradually increasing current to deposit platinum multilayers of varying thickness on the surface of the implanted samples. Ion beam milling was performed at 30 kV and 93 pA followed by a final clean using a 5 kV Ga beam current of 12 pA to remove surface material deposited during FIB and to remove the residual FIB milling damage. Care was taken to minimize the ion beam interaction with the exposed surface throughout the TEM sample preparation. TEM imaging was done at the National Renewable Energy Laboratory (NREL) using an FEI Tecnai operating at 300 kV in TEM mode. Images were collected using a Gatan Osiris CCD camera. Samples were imaged using a 10-40 μm objective aperture, depending on sample thickness. Selected area electron diffraction (SAED) patterns were utilized to identify the irradiated region when the irradiated band could not be identified visually. Helium bubbles were imaged using the through-focusing technique, in which Fresnel contrast produces a white spot with a dark ring in under-focus conditions and a dark spot with a white ring in over-focus. The image was defocused in series from $-1.5 \mu\text{m}$ to $+1.5 \mu\text{m}$ at the SRIM predicted He peak location to confirm the presence or absence of helium bubbles.

Helium bubbles were quantified using the 'Analyze Particle' feature in ImageJ [25], an open platform for scientific image analysis. TEM images were imported into ImageJ, where a standard

procedure was developed for quantifying the total bubble cross-sectional area. Images were first color inverted using “Image Inverter,” then filtered using “Fast Filters” set to a median filter type with x and y radii of 30, preprocessing was set to “smooth” and subtract filtered checked. The subtraction offset was set to 170. These inversion and filtering steps act to create high contrast between the helium bubbles and defect-fluorite background present in the image. “Color Threshold” was then utilized to highlight the bubbles in red. In order to highlight only the bubbles, the brightness bar was adjusted. After calibrating the image from pixels to nanometers using the scale bar, “Analyze Particles” was set to measure particle sizes 10-100 nm² with any range of circularity (due to the helium bubble chains that formed in this study). ImageJ provides the cross-sectional area of each bubble in nm², which was then converted to bubble radius using a circular cross-sectional area approximation. Since some bubbles formed long chains, the circular approximation is not true in all cases. The helium bubble number density was calculated by counting bubbles inside seven 50 × 50 nm squares from inside the main band of helium bubbles in the under-focused image. Since the bubbles might be present anywhere throughout the volume of the TEM foil, the number density was calculated by estimating the foil thickness (~100 nm), using a total volume of 2.5 × 10⁵ nm³ for each square. The volume swelling due to helium bubbles was estimated based on the bubble density and the average bubble volume.

2.2.4. Swelling and bubble formation in Gd₂Zr₂O₇

In the Gd₂Zr₂O₇ samples implanted with peak concentrations of 0.1 and 1.0 at% helium, the GXR D results show a shift of each reflection towards lower 2θ positions, as illustrated in Fig. 18 for the sample containing 1 at% helium. These results indicate a somewhat uniform strain that increases with depth and helium content in samples implanted with 0.1 and 1.0 at% helium. However, in the sample with a peak concentration of 12 at%, both unstrained defect-fluorite and strained peaks appear at depths corresponding to the implanted helium, as shown in Fig. 19 for the (220) peak. This indicates that local regions with and without lattice strain exist at depths greater than ~100 nm from the surface. This suggests the presence of relaxed regions within the irradiated region that are not present at lower helium concentrations. The unit cell volume expansion in this sample, as a function of X-ray penetration depth, is shown in Fig. 20. The

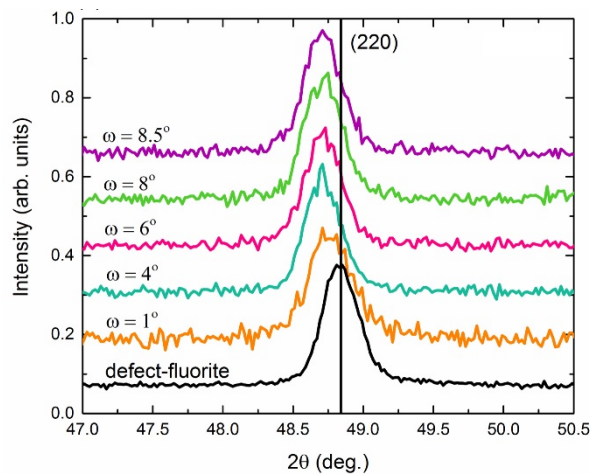


Fig. 18. Magnified (220) peak for Gd₂Zr₂O₇ with 1 at% He for various grazing angles.

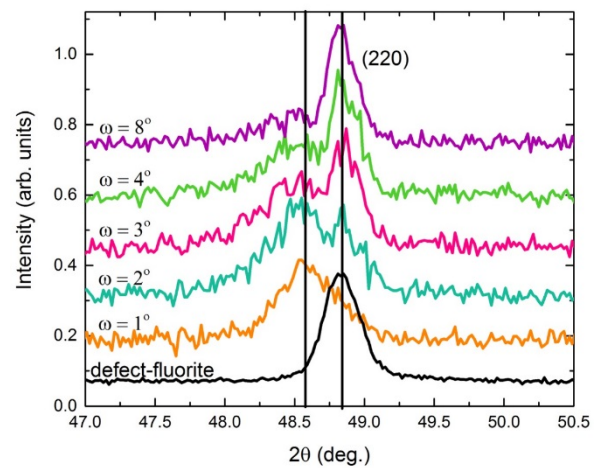


Fig. 19. Magnified (220) peak for Gd₂Zr₂O₇ with 12 at% He for various grazing angles.

maximum swelling from the accumulation of helium is about 3%.

In the sample implanted with 12 at% He, uniform helium accumulation, but no bubble nucleation, occurred throughout the lattice from the surface to a depth of ~ 150 nm (Fig. 21), resulting in single strained peak at a grazing angle of $\omega = 1^\circ$ in Fig. 19. At depths between 150 and 200 nm, corresponding to a grazing angle of $\omega = 2^\circ$, isolated 1 to 3 nm diameter bubbles were observed in the TEM micrographs, as shown in Fig. 21, with bubbles first forming at a depth of 165 nm, corresponding to 4.6 at% helium when

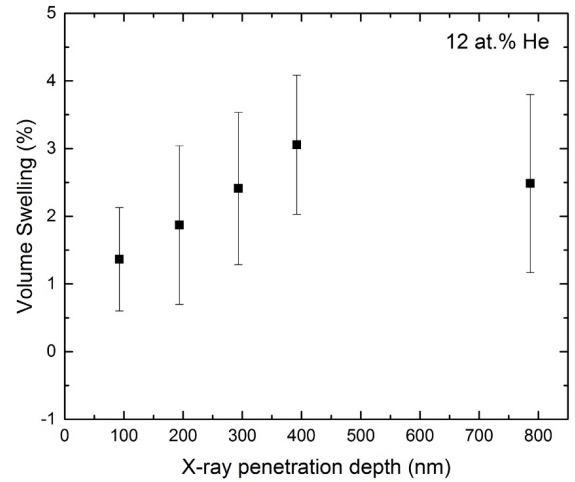


Fig. 20. Unit cell volume expansion as a function of X-ray penetration depth in Gd₂Zr₂O₇ implanted with 12 at% He.

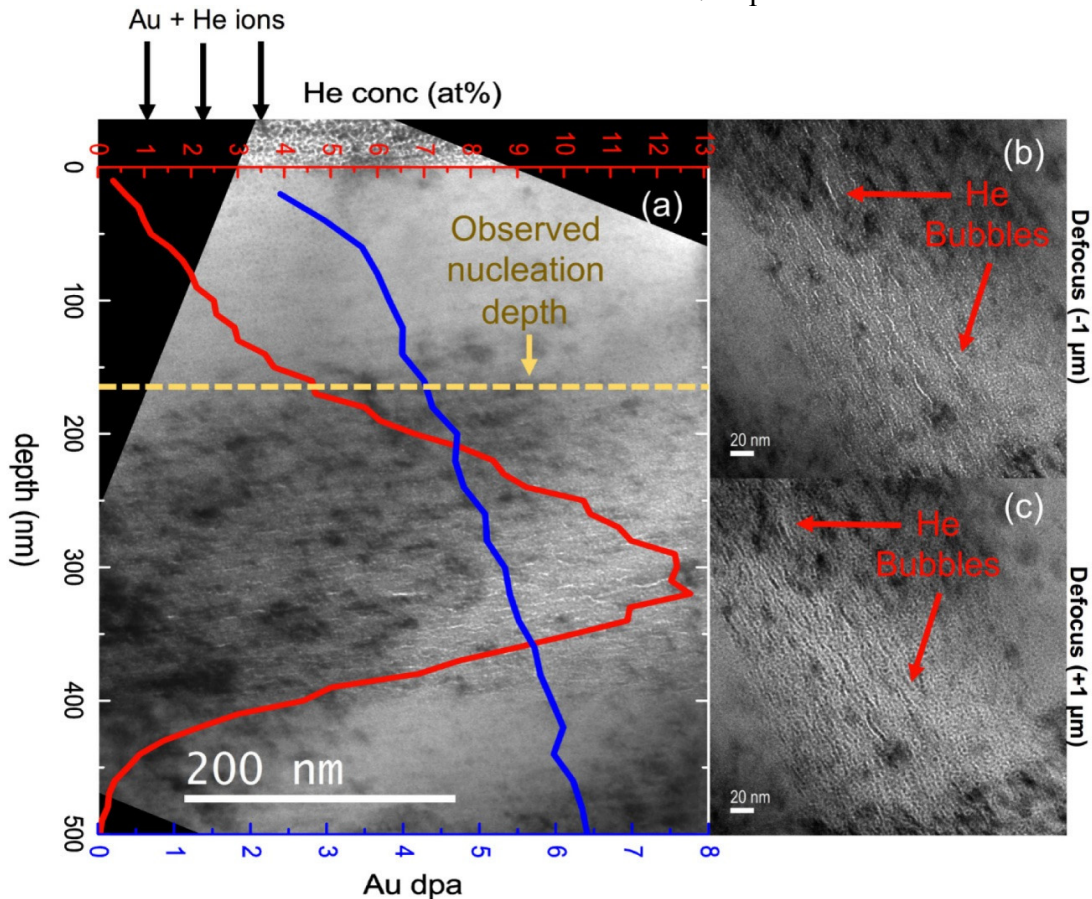


Fig. 21. TEM images for Gd₂Zr₂O₇ irradiated with 7 MeV Au³⁺ to 2.2×10^{15} ions/cm² and then implanted with 65 keV He⁺ to 2×10^{17} ions/cm² (12.7 at% helium at peak). Helium concentration and Au damage distributions from SRIM are overlaid in (a). Images obtained at defocus values of ± 1 μ m: (b) under-focus and (c) over-focus. Bubbles are observed to first form at a depth of 165 nm (yellow dotted line), corresponding to 4.6 at% helium.

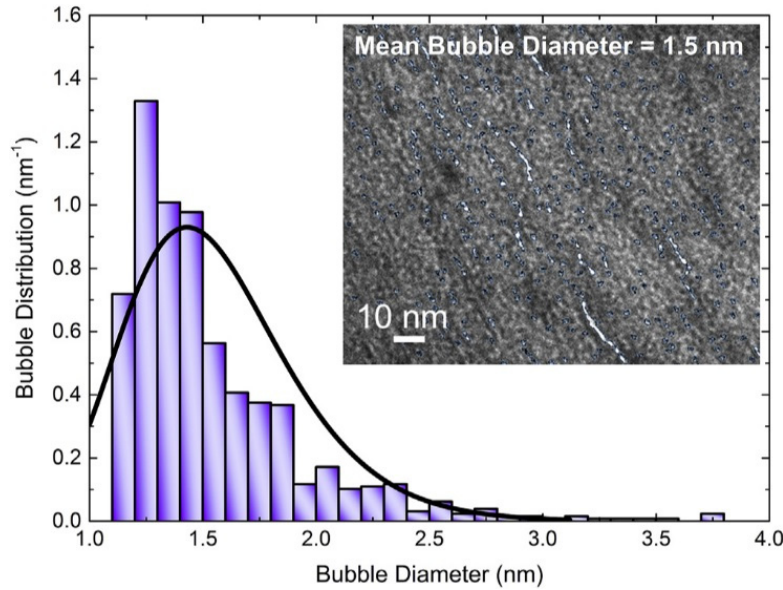


Fig. 22. Helium bubble size distribution in sample implanted with 12 at% He at the peak. The line fit is a log-normal distribution with a mean of 1.5 ± 0.2 nm. Inset shows outlines of bubbles from ImageJ analysis overlaid on the original under-focused TEM image shown in Fig. 21 (b).

compared to SRIM predictions. At this X-ray penetration depth, the strained peak in Fig. 19 exhibited higher intensity than the defect-fluorite peak. At a depth range of 200 to 400 nm, isolated 1 to 3 nm bubbles were still present, but some bubbles coalesced to form chains that were 10 to 30 nm in length, clearly observed in the TEM micrograph in Fig. 21. This corresponds to the regions where the defect-fluorite peak increased in intensity beyond the strained peak ($\omega = 3-4^\circ$ in Fig. 19). Since the defect-fluorite peak increased in intensity with respect to the strained peak at depths where the helium bubbles began to coalesce into chains, the reorganization of helium bubbles into chains seems to produce more relaxation of the strain in the crystalline lattice than the simply random nucleation of isolated bubbles. Helium bubbles are not observed in any of the samples at lower helium concentrations. The TEM images also show line defects in the sample, where the helium irradiation produced an additional 4.5 dpa beyond the pre-damage level. These line defects are believed to be dislocations, but additional work is required to determine their true nature.

The bubble size distribution obtained from the analysis of the TEM micrographs is shown in Fig. 22. Most bubbles were observed to be 1.1 to 1.6 nm in diameter. The bubble number density was $1.8 \pm 0.4 \times 10^{-4}$ bubbles/nm³. The volume swelling due to helium bubbles is estimated to be between 0.06 and 0.2 %, which is significantly less than that due to lattice strain.

Previous literature results on single crystal and polycrystalline yttria-stabilized zirconia (YSZ) [17,26], which has a defect-fluorite crystal structure like Gd₂Zr₂O₇ after irradiation up to 0.4 dpa, show helium bubbles and bubble chains parallel to the surface forming at 2×10^{17} ions/cm², which is the same fluence where bubbles and chains are observed in this work for Gd₂Zr₂O₇. Yang *et al.* [26] measured the normal strain due to helium irradiation in YSZ single crystals using high resolution x-ray diffraction (HRXRD) and found an increase in normal strain after

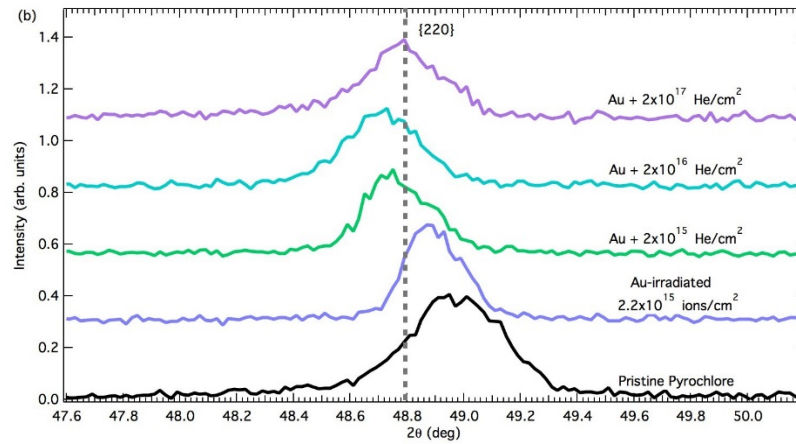


Fig. 23. GIXRD at an incident angle of $\omega = 6^\circ$ for the $\{220\}$ reflection from $\text{Gd}_2\text{Zr}_2\text{O}_7$ samples pre-damaged with 7 MeV Au^{3+} to 2.2×10^{15} ions/cm², and pre-damaged $\text{Gd}_2\text{Zr}_2\text{O}_7$ implanted with 200 keV He^+ ions to fluences of 2×10^{15} , 2×10^{16} , and 2×10^{17} ions/cm².

irradiation with 1×10^{16} ions/cm², and again after 8×10^{16} ions/cm², but an almost complete disappearance of normal strain after irradiation with 2×10^{17} ions/cm², the fluence where bubbles and bubble chains were first observed. This indicates that bubble chains form in order to reduce the strain normal to the surface, which is produced due to radiation damage accumulation. In this study, we wanted to study strain at various helium fluences to see if helium bubble chains form by a similar mechanism in $\text{Gd}_2\text{Zr}_2\text{O}_7$. $\text{Gd}_2\text{Zr}_2\text{O}_7$ single crystals are not easily obtained, so HRXRD could not be utilized for this work. Instead, lattice parameter changes were determined for each irradiation condition using grazing incidence x-ray diffraction (GIXRD), as shown in Fig. 23. In this experiment, $\text{Gd}_2\text{Zr}_2\text{O}_7$ was pre-damaged and then irradiated with 200 keV He to either 2×10^{15} , 2×10^{16} or 2×10^{17} ions/cm². Four grazing angles were used; $\omega = 1^\circ$, 4° , 6° , and 8° , which correspond to x-ray penetration depths of roughly 100, 400, 600, and 800 nm. Clear peak shifts were observed for each irradiation condition, as shown in Fig. 23.

Peaks shifted to lower 2θ after the pre-damage and after implantation with 2×10^{15} and 2×10^{16} , indicating lattice expansion, but shifted back to a higher 2θ after implantation with 2×10^{17} ions/cm². The lattice parameters were calculated using four fluorite reflections for each irradiation condition and grazing angle, as shown in Fig. 24.

Less variation occurred between the different reflections in the Au irradiated sample (Fig. 24 (a)) than in the pre-damaged and He implanted samples (Figs. 24 (b-d)). In GIXRD, the beam enters the detector at a different angle with respect to the surface normal for each reflection, so variation in lattice parameter for different reflections likely indicates an anisotropic strain distribution. Trends in the lattice parameter calculations indicate an increase in lattice parameter for the pre-damaged sample and the samples pre-damaged and implanted with 2×10^{15} and 2×10^{16} ions/cm², but a decrease in lattice parameter in the sample pre-damaged and implanted with 2×10^{17} ions/cm², as shown in Fig. 25. The lattice parameter decrease measured in the 2×10^{17} ions/cm² sample indicates that some lattice strain may have been relieved due to the formation of He bubble chains. Thus, bubble chains may be forming in order to reduce the total strain in $\text{Gd}_2\text{Zr}_2\text{O}_7$, similar to previous studies in the literature on YSZ.

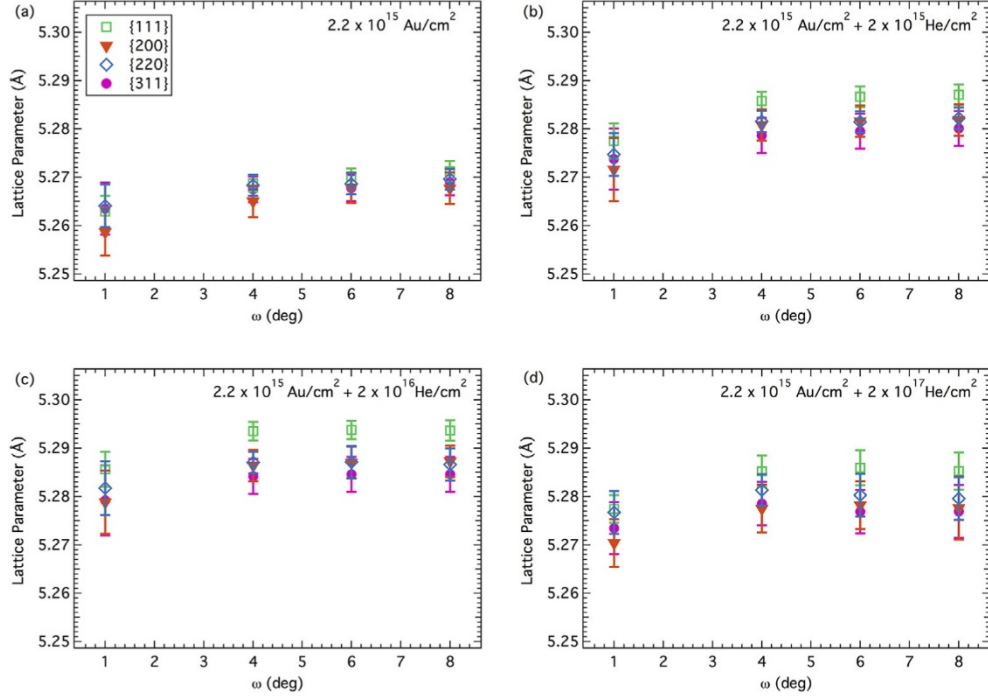


Fig. 24. Lattice parameters determined from GIXRD data using the four most intense fluorite reflections: (a) Au irradiated sample; (b-d) Au irradiated (pre-damaged) and He implanted samples.

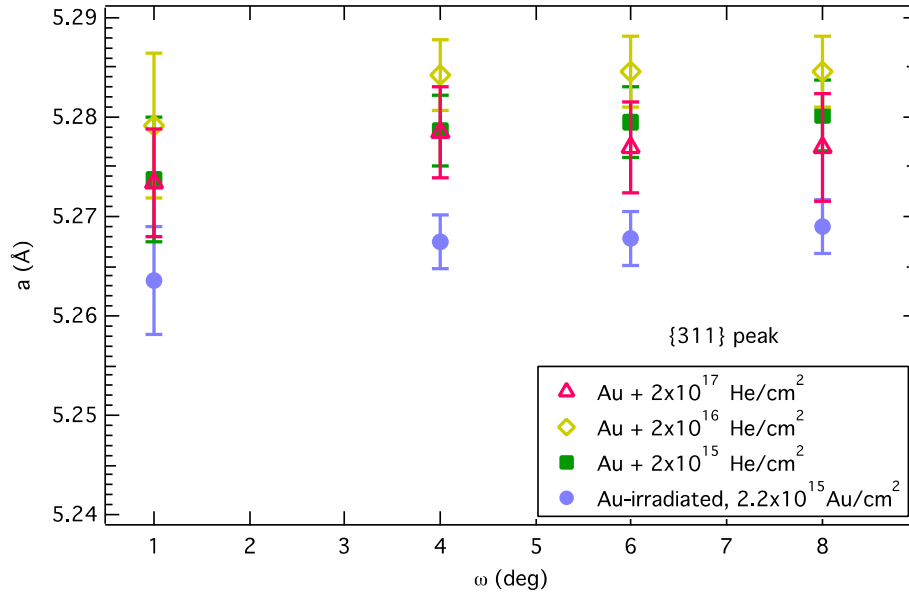


Fig. 25. Experimentally determined lattice parameters for $\text{Gd}_2\text{Zr}_2\text{O}_7$ samples implanted with 200 keV He^+ relative to the pre-damaged (Au irradiated) sample for various incident x-ray angles. Lattice parameters were calculated using the fluorite {311} reflection. Error bars represent the fractional error.

In summary, this work, which has been published [27], shows that $\text{Gd}_2\text{Zr}_2\text{O}_7$, often considered the most radiation resistant pyrochlore, is susceptible to nucleation of He bubbles and concomitant volume swelling. The threshold helium concentration for bubble formation is estimated to be 4.6 at% in defect-fluorite $\text{Gd}_2\text{Zr}_2\text{O}_7$.

2.2.5. Bubble Formation in $\text{Gd}_2\text{Ti}_2\text{O}_7$

The irradiated $\text{Gd}_2\text{Ti}_2\text{O}_7$ samples were characterized using TEM to quantify the presence or absence of bubbles using the through-focus technique. Each sample was imaged in the TEM while focused, and at all defocus values between $-1\text{ }\mu\text{m}$ and $+1\text{ }\mu\text{m}$. Several magnifications were utilized to search for bubbles. The TEM image was focused by expanding the Fourier transform to the largest possible diameter. Defocus values may vary by an estimated $\pm 100\text{ nm}$ due to error in finding the zero (focused) point. In under-focus conditions, bubbles or voids appear bright with a dark ring; while in over-focus conditions, the bubbles appear dark with a bright ring, due to Fresnel contrast. All TEM imaging used the smallest possible objective aperture (ranging from 20-60 μm). Helium bubbles were not observed in $\text{Gd}_2\text{Ti}_2\text{O}_7$ samples irradiated with Au and implanted with 2×10^{16} He ions/ cm^2 , even after subsequent Au ion irradiations at up to 700 K.

To study $\text{Gd}_2\text{Ti}_2\text{O}_7$ samples implanted with 2×10^{17} He ions/ cm^2 , FIB lamella were taken from

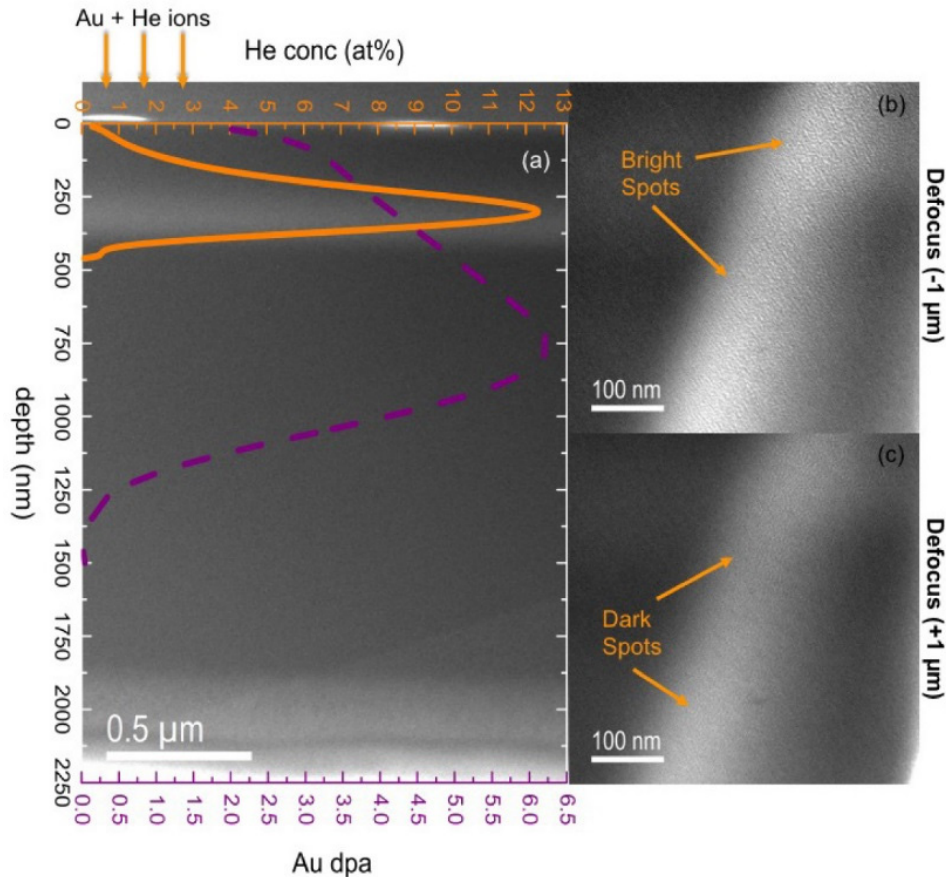


Fig. 26. TEM images of $\text{Gd}_2\text{Ti}_2\text{O}_7$ irradiated with 2.2×10^{15} Au ions/ cm^2 and 2×10^{17} He ions/ cm^2 . Overview of irradiated region shown in (a), dashed (purple) line corresponds to Au dpa. Through-focusing at the helium implant peak shows bubbles as (b) bright spots for under-focus and as (c) dark spots for over-focus.

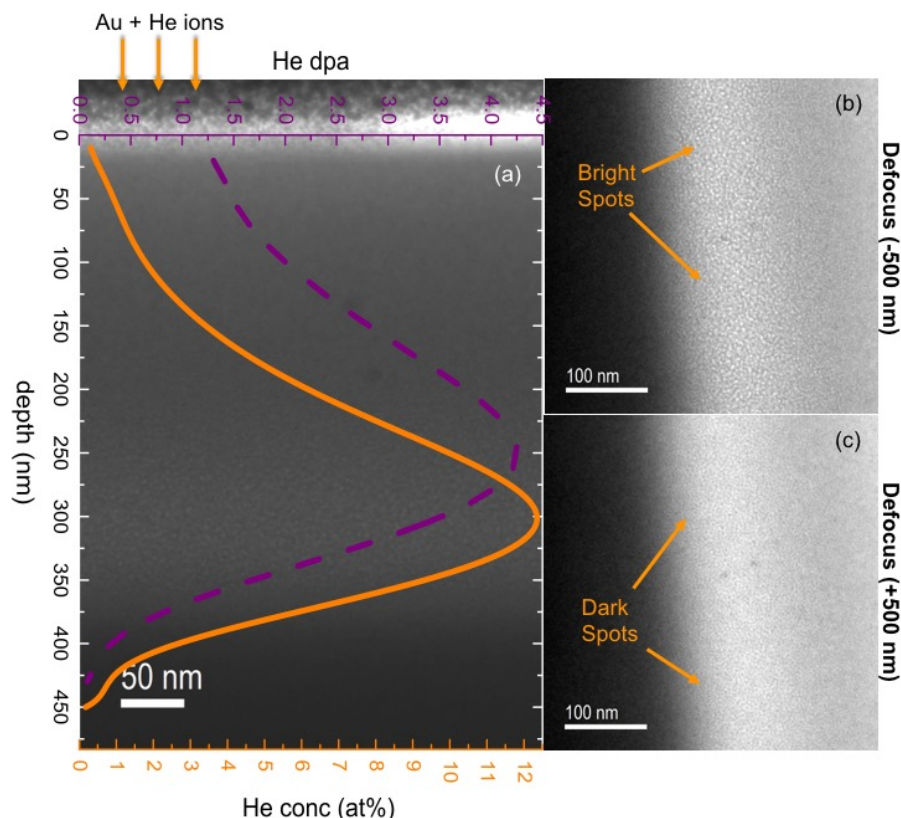


Fig. 27. TEM images of pristine $\text{Gd}_2\text{Ti}_2\text{O}_7$ implanted with 2×10^{17} He ions/ cm^2 . Overview of irradiated region shown in (a), dashed (purple) line corresponds to He dpa. Through-focusing at the helium implant peak: (b) bubbles as bright spots for under-focus and (c) as dark spots for over-focus.

the center of the sample (Fig. 26), where the sample was irradiated with Au and implanted with He, and from the edge of the sample (Fig. 27), where the sample was not irradiated with Au, but was implanted with He. In the $\text{Gd}_2\text{Ti}_2\text{O}_7$, He bubbles were observed after an implantation fluence of 2×10^{17} He/ cm^2 in both the amorphous implanted structure (Fig. 26) and in the pristine implanted structure (Fig. 27). The bubbles ranged in size from 1 to 4 nm in diameter, with the average bubble size being larger in the pristine implanted sample than in the amorphous (Au-irradiated) implanted sample. As noted, helium bubbles were quantified using the ImageJ software [25], which determines the approximate cross-sectional area of each bubble. For the case of the pristine $\text{Gd}_2\text{Ti}_2\text{O}_7$ implanted with 2×10^{17} He ions/ cm^2 , specifically the region shown in Fig. 27 (b), the bubble outlines generated by ImageJ for analysis are illustrated in Fig. 28. Because of the low contrast between bubbles and the amorphous $\text{Gd}_2\text{Ti}_2\text{O}_7$ makes image analysis difficult, the image analysis is subjective, and results should only be utilized as a qualitative guide for understanding bubble density and size. The cross-sectional area of each bubble was converted to bubble diameter using a circular cross-sectional area approximation. Most bubbles observed in these samples were close to spherical. The bubble size distributions, which were fit with a log-normal distribution to determine the average diameter, are shown in Fig. 29 for the pre-damaged $\text{Gd}_2\text{Ti}_2\text{O}_7$ implanted with 2×10^{17} He ions/ cm^2 and in Fig. 30 for the pristine $\text{Gd}_2\text{Ti}_2\text{O}_7$ implanted with 2×10^{17} He ions/ cm^2 . The mean bubble diameter is 1.5 nm in the pre-

damaged and He implanted sample (Figs. 26) and 2.1 nm in the pristine sample implanted with just helium (Figs. 27). The error in bubble diameter was estimated as 0.2 nm based on the TEM image pixel size, which was 0.2 nm in the TEM images for both the pre-damaged sample implanted with 2×10^{17} He/cm² and the pristine sample implanted with 2×10^{17} He/cm².

In this study, which has been published [28], the He concentration (~ 6 at%) required for observable bubble nucleation in pre-damaged (amorphous) Gd₂Ti₂O₇ is about a factor of 2 larger than the critical He concentration of 3 at% estimated for observable bubble formation in amorphous borosilicate glass [29]. While bubbles 1-2 nm in diameter have been observed at concentrations as low as 0.12 at% in borosilicate glass [30], bubbles are not observed in pre-damaged Gd₂Ti₂O₇ implanted with 2×10^{16} He/cm² (peak He concentration of 1 at%), even after subsequent post-implantation irradiation at 300, 500 and 700 K. Bubbles are barely visible in the sample pre-damaged and implanted with 2×10^{17} He/cm². Since bubbles are not observed in the sample pre-damaged, implanted with 2×10^{16} He/cm², and post-damaged at both room and high temperature, the additional irradiation damage does not appear to enhance He mobility or bubble nucleation in the pre-damaged Gd₂Ti₂O₇ containing up to 1 at% He. Thermally induced He mobility in

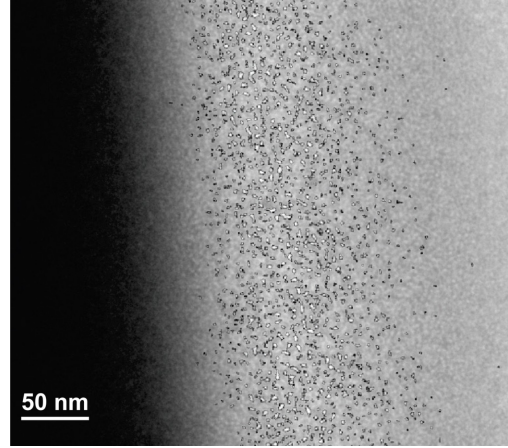


Fig. 28. Bubble outlines from ImageJ analysis of the pristine Gd₂Ti₂O₇ implanted with 2×10^{17} He/cm², the region in Fig. 27 (b).

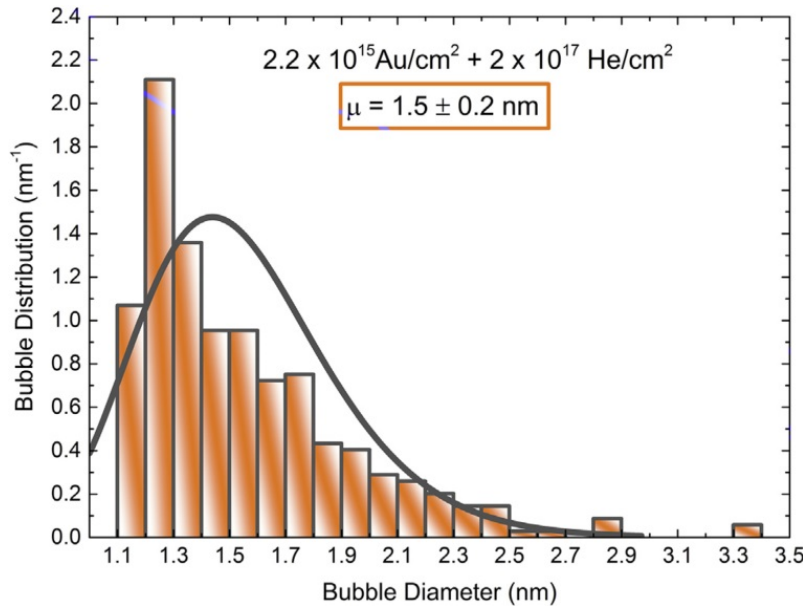


Fig. 29. Bubble size distribution for Gd₂Ti₂O₇ irradiated with 2.2×10^{15} Au ions/cm² and implanted with 2×10^{17} He ions/cm². The line fit shows a log-normal distribution with a mean of 1.5 ± 0.2 nm.

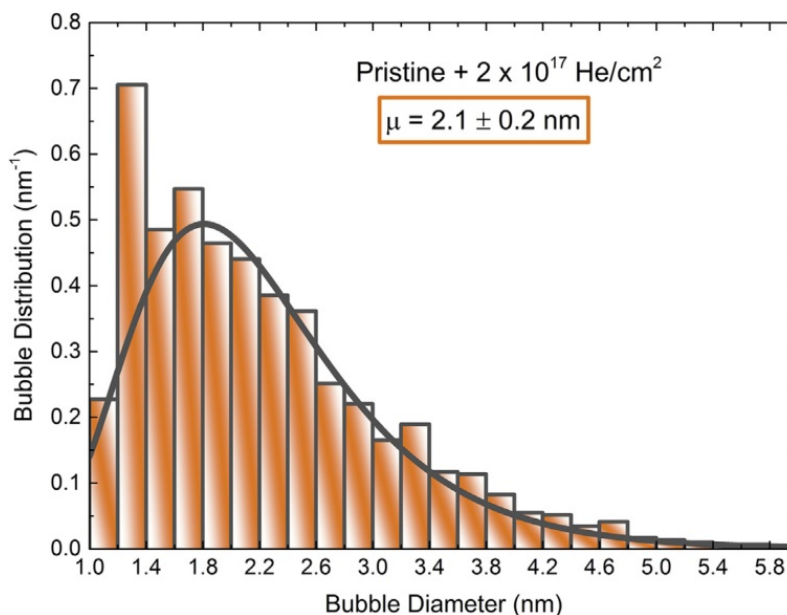


Fig. 30. Bubble size distribution for $\text{Gd}_2\text{Ti}_2\text{O}_7$ implanted with 2×10^{17} He ions/ cm^2 . The line fit shows a log-normal distribution with a mean of 2.1 ± 0.2 nm.

amorphous $\text{Gd}_2\text{Ti}_2\text{O}_7$ seems to remain low at 700 K, which agrees with the He desorption work performed by Wiss et al. [31] on partially amorphous and fully amorphous $\text{Gd}_2\text{Ti}_2\text{O}_7$, where He release did not occur until a temperature of 900 K was reached. The first desorption peak for the crystalline structures $\text{Gd}_2\text{Zr}_2\text{O}_7$ and $\text{Nd}_2\text{Zr}_2\text{O}_7$ occurred at 700 K, lower than the amorphous $\text{Gd}_2\text{Ti}_2\text{O}_7$ structure, which suggests a higher He mobility in crystalline pyrochlore than in amorphous pyrochlore. In this work, bubbles are larger and of higher density in pristine implanted $\text{Gd}_2\text{Ti}_2\text{O}_7$ than in amorphous implanted $\text{Gd}_2\text{Ti}_2\text{O}_7$, suggesting a higher He mobility in the pristine lattice. In the early stages (prior to amorphization) of He implantation into pristine $\text{Gd}_2\text{Ti}_2\text{O}_7$, the He may be more mobile than in amorphous $\text{Gd}_2\text{Ti}_2\text{O}_7$, leading to the formation of larger bubbles in the pristine implanted sample. Bubbles appeared circular in both samples implanted with 2×10^{17} He/ cm^2 , which is the morphology common to amorphous materials implanted with He.

3. Summary

This research has advanced the understanding on the effects of self-radiation from alpha decay on the response of used nuclear fuel and nuclear waste forms during high-temperature interim storage and long-term permanent disposition. The research has employed novel irradiation approaches, based on separate and sequential irradiations with heavy ions and helium ions over a range of temperatures, to investigate the separate and integrated effects of irradiation and helium accumulation on microstructure evolution in model used nuclear fuel and nuclear waste form materials. These results provide structural evolution boundaries on helium bubble formation that can ultimately affect radionuclide release to the environment, once canisters are breached and interactions with the geological environment commence. This research has provided critical

training to students and early-career researchers on designing irradiation experiments and in evaluating the performance of used nuclear fuels and waste forms.

Beta decay is not expected to affect the performance of used nuclear fuel; however, alpha decay will result in the accumulation of helium that will form helium bubbles once the helium concentration exceeds about 0.15 at% helium, which will occur within 100, 1000 or 10,000 years for MOX, high-burnup or current commercial used fuels, respectively. However, due to the rim-effect in high-burnup nuclear fuels, bubble formation may be greatly accelerated and substantially higher in the rim region of nuclear fuel pellets because the local burnup is much higher (factor of two or more) than the average burnup reported for used nuclear fuel [5], which could lead to possible fragmentation of the outer rim on geologic time scales.

While benchmark data have not yet been obtained on helium bubble formation in ^{238}Pu -doped or ^{244}Cm -doped ceramic waste forms for comparison, the results from this project indicate that helium bubble formation will not occur in these materials until the helium content exceeds 4 to 6 at%. Therefore, helium bubble formation is not expected to occur in any pyrochlore-based ceramic waste form for at least 100,000 years.

4. References

1. E. Maugeri, T. Wiss, J.-P. Hiernaut, K. Desai, C. Thiriet, V.V. Rondinella, J.-Y. Colle, R.J.M. Konings, *J. Nucl. Mater.* **385** (2009) 461.
2. D. Staicu, T. Wiss, V.V. Rondinella, J.P. Hiernaut, R.J.M. Konings, C. Ronchi, *J. Nucl. Mater.* **397** (2010) 8.
3. C. Poinssot, S. Gin, *J. Nucl. Mater.* **420** (2012) 182.
4. T. Wiss, J.-P. Hiernaut, D. Roudil, J.-Y. Colle, E. Maugeri, Z. Talip, A. Janssen, V. Rondinella, R. J. M. Konings, Hj. Matzke, and W. J. Weber, *J. Nucl. Mater.* **451** (2014) 198.
5. J. Spino, H. Santa Cruz, R. Jovani-Abril, R. Birtcher, and C. Ferrero, *J. Nucl. Mater.* **422** (2012) 27.
6. W. J. Weber, R. C. Ewing, C. R. A. Catlow, T. Diaz de la Rubia, L. W. Hobbs, C. Kinoshita, Hj. Matzke, A. T. Motta, M. Nastasi, E. K. H. Salje, E. R. Vance, and S. J. Zinkle, *J Mater. Res.* **13** (1998) 1434.
7. R.C. Ewing, W.J. Weber, J. Lian, *J. Appl. Phys.* **95** (2004) 5949.
8. M. Kato et al., *J. Nucl. Mater.* **393** (2009) 134.
9. Y. Tahara et al. *Nucl. Instrum. Meth. Phys. Res. B* **269** (2011) 886.
10. M. Kinoshita, *Nucl. Instrum. Meth. Phys. Res. B* **267** (2009) 960.
11. A. Oaks et al. *J. Nucl. Mater.* **414** (2011) 145.
12. Y. Zhang, M. L. Crespillo, H. Xue, K. Jin, C.-H. Chen, C. L. Fontana, J. T. Graham, and W. J. Weber, *Nucl. Instrum. Meth. Phys. Res. B* **338** (2014) 19.
13. Y. Zhang, W. Jiang, C. Wang, F. Namavar, P. D. Edmondson, Z. Zhu, F. Gao, J. Lian, and W. J. Weber, *Phys. Rev. B* **82** (2010) 184105.

14. Y. Zhang, P. D. Edmondson, T. Varga, S. Moll, F. Namavar, C. Lan, and W. J. Weber, *Phys. Chem. Chem. Phys.* **13** (2011) 11946.
15. J. Spino and D. Papaioannou, *J. Nucl. Mater.* **372** (2008) 416.
16. T. Wiss, O. Dieste-Blanco, A. Tacu, A. Janssen, Z. Talip, and J.-Y. Colle, *J. Mater. Res.* **30** (2015) 1544.
17. T. Yang, C. A. Taylor, C. Wang, Y. Zhang, W. J. Weber, J. Xiao, J. Xue, S. Yan, and Y. Wang, *J. Amer. Ceram. Soc.* **98** [4] (2015) 1314.
18. W. B. Lacina and P. S. Perhan, *Phys. Rev. B.* **1** [4] (1969) 1765.
19. A. Nakajima, A. Yoshihara and M. Ishigame, *Phys. Rev. B.* **50** [18] (1994) 13297.
20. H. Richter, Z. P. Wang and L. Ley, *Solid State Commun.* **39** (1981) 625.
21. R. Shuker and R. W. Gammon, *Phys. Rev. Lett.* **25** (1970) 222.
22. K. K. Tiong, P. M. Amirtharaj and F. H. Pollak, *Appl. Phys. Lett.* **44** [1] (1984) 122.
23. E. H. Martins Ferreira, M. V. O. Moutinho, F. Stavale, M. M. Lucchese, R. B. Capaz, C. A. Achete and A. Jorio, *Phys. Rev. B.* **82** (2010) 125429.
24. B.H. Toby, *J. Appl. Crystall.* **38** (2005) 1040.
25. W.S. Rasband, *ImageJ*, <http://imagej.nih.gov/ij/>.
26. T. Yang, X. Huang, Y. Gao, C. Wang, Y. Zhang, J. Xue, S. Yan, Y. Wang, *J. Nucl. Mater.* **420** (2012) 430.
27. C.A. Taylor, M.K. Patel, J.A. Aguiar, Y. Zhang, M.L. Crespillo, J. Wen, H. Xue, Y.Q. Wang, and W.J. Weber, *Acta Materialia* **115** (2016) 115.
28. C. A. Taylor, M. K. Patel, J. A. Aguiar, Y. Zhang, M. L. Crespillo, J. Wen, H. Xue, Y. Q. Wang, and W. J. Weber, *J. Nucl. Mater.* **479** (2016) 542.
29. G. Gutierrez, S. Peugeot, J.A. Hinks, G. Greaves, S.E. Donnelly, E. Oliviero, C. Jegou, *J. Nucl. Mater.* **452** (2014) 565-568.
30. R. Bes, T. Sauvage, S. Peugeot, J. Haussy, F. Chamssedine, E. Oliviero, T. Fares, L. Vincent, *J. Nucl. Mater.* **443** (2013) 544.
31. T.A.G. Wiss, J.P. Hiernaut, P.M.G. Damen, S. Lutique, R. Fromknecht, W.J. Weber, *J. Nucl. Mater.* **352** (2006) 202.